Article

Analysis of the Structure, Thermal, and Molecular Dynamics of Organic−Inorganic Hybrid Crystal at Phases IV, III, II, and I: [NH$_2$(CH$_3$)$_2$]$_2$CdBr$_4$

Sun Ha Kim, Yong Lak Joo, and Ae Ran Lim*

Read Online

ACCESS | Metrics & More | Article Recommendations | SI Supporting Information

ABSTRACT: A comprehensive understanding of the physicochemical properties of organic−inorganic hybrids is essential for their solid-state lighting applications. Therefore, a single crystal of [NH$_2$(CH$_3$)$_2$]$_2$CdBr$_4$ was grown; the crystal structure was monoclinic, and the phase transition temperatures for the four phases IV, III, II, and I were 383 K (T_{C1}), 417 K (T_{C2}), and 427 K (T_{C3}). Furthermore, the chemical shifts caused by the local field around ^{1}H, ^{13}C, ^{14}N, and ^{113}Cd changed continuously with temperature, especially near T_{C1}, indicating that the local environment changes with temperature. Owing to the large change in ^{113}Cd chemical shifts, the coordination geometry of Br around Cd in the CdBr$_4$ tetrahedra changes near T_{C1}. Therefore, it is proposed that Br plays a significant role in the N−H···Br hydrogen bond. Finally, the spin-lattice relaxation time $T_{1\rho}$, representing the energy transfer around the ^{1}H and ^{13}C atoms of the cation, changed significantly with temperature. The activation energies obtained from the $T_{1\rho}$ results were two times larger at high temperatures than at low temperatures. This study provides an understanding of the fundamental properties of organic−inorganic hybrid compounds to broaden their applications.
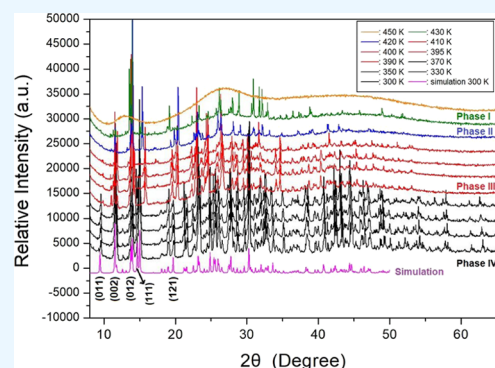
1. INTRODUCTION

Organic−inorganic hybrid compounds are of great interest for various applications such as sensors, fuel cells, solar cells, light-emitting transistors, and light-emitting diodes.[1−4] Additionally, organic−inorganic hybrid perovskite materials are applied in ferroelectrics, dielectric switches, and optical switches.[5−11] Recently, CH$_3$NHPbX$_3$ (X = Cl, Br, I) has been used for solar cells, but these materials are easily degraded in humid air and are toxic because of the presence of Pb. Therefore, the development of eco-friendly hybrid perovskite solar cells is urgently required.[12−16] As new alternatives, two-dimensional compounds such as [NH$_3$(CH$_2$)$_n$NH$_3$]MX$_4$ (n = 1, 2, 3,...; M^{2+} = divalent transition metal, Mn, Co, Cu, Zn, Cd, or Pb; X = halogen, Cl, Br, or I)[17−28] and [(C$_n$H$_{2n+1}$NH$_3$)]$_2$MX$_4$ are examples of organic−inorganic hybrids that have recently attracted considerable attention.[29−37] Moreover, it is necessary to study the hydrogen-bond structure of [NH$_2$(CH$_3$)$_n$]$_2$MX$_4$,[38−44] which is different than that of [NH$_3$(CH$_2$)$_n$NH$_3$]MX$_4$ with three H atoms bonded to one N.

One of these alternatives, dimethylammonium tetrabromo-cadmate (II), [NH$_2$(CH$_3$)$_2$]$_2$CdBr$_4$,[38,39] is a member of [NH$_2$(CH$_3$)$_n$]$_2$MX$_4$, which belongs to the A$_2$MX$_4$ group, where A$^+$ is a univalent cation. These crystals undergo several structural phase transitions, which are commonly associated with the ordering of hydrogen bonds and the corresponding changes in the molecular dynamics of [NH$_2$(CH$_3$)$_2$]$^+$ ions. The individual MX$_4$ tetrahedral anions in these materials are

completely isolated and surrounded by organic [NH$_2$(CH$_3$)$_2$]$^+$ cations. Recently, increased interest in the hybrids based on the halo-Cd hybrids has been observed due to their photoluminescent properties. Specifically, these materials exhibit white-light emission, rendering them suitable potential light sources for solid-state lighting applications. Also, some representatives of halogenocadmate (II) hybrids display semiconducting properties, making them applicable in color lighting or displays.

[NH$_2$(CH$_3$)$_2$]$_2$CdBr$_4$ was demonstrated to undergo three structural phase transitions at 380, 413, and 426 K.[39] At 300 K, the [NH$_2$(CH$_3$)$_2$]$_2$CdBr$_4$ crystal exhibited a monoclinic structure with a $P2_1/n$ space group and its lattice constants were a = 8.158 Å, b = 11.632 Å, c = 15.166 Å, β = 94.82°, and Z = 4.[38] The structure consisted of [CdBr$_4$]$^{2+}$ anions and nonequivalent [NH$_2$(CH$_3$)$_2$](1) and [NH$_2$(CH$_3$)$_2$](2) cations. The structure comprised infinite chains of face-sharing CdBr$_4$ tetrahedra with the [NH$_2$(CH$_3$)$_2$]$^+$ ions located in the free space between the chains. Notably, the slightly deformed

CdBr$_4$ tetrahedra were linked to organic [NH$_2$(CH$_3$)$_2$] cations via N−H···Br hydrogen bonds.[38]

In this study, single crystals of [NH$_2$(CH$_3$)$_2$]$_2$CdBr$_4$ are grown using an aqueous solution method, and their structures and phase transition temperatures (T_C) are characterized using single-crystal X-ray diffraction (XRD), powder XRD, and differential scanning calorimetry (DSC). Additionally, thermogravimetry analysis (TGA) is performed to gain a better understanding of the thermal properties of the samples. To characterize the coordination geometry of the ^{1}H, ^{13}C, ^{14}N, and ^{113}Cd atoms in the samples, ^{1}H magic-angle spinning nuclear magnetic resonance (MAS NMR), ^{13}C MAS NMR, ^{14}N static NMR, and ^{113}Cd static NMR chemical shifts are obtained as a function of temperature. Based on the results, the N−H···Br hydrogen bond between the cation and anion is discussed. Moreover, ^{1}H and ^{13}C spin-lattice relaxation times $T_{1\rho}$ representing the energy transfer around the ^{1}H and ^{13}C atoms of the cation are discussed, and their activation energies E_a are determined. The results of the single-crystal structure and physicochemical properties are predicted to provide important information on the fundamental mechanism of organic−inorganic hybrid compounds.

2. RESULTS AND DISCUSSION

2.1. Crystal Structure. Single-crystal XRD results for the [NH$_2$(CH$_3$)$_2$]$_2$CdBr$_4$ crystal were obtained at 300 K. The synthesized crystal had a monoclinic system with a $P2_1/n$ space group, and lattice constants of a = 8.2528 (9) Å, b = 11.7833 (14) Å, c = 15.3589 (18) Å, β = 94.726°, Z = 4 (CCDC number 2256555). The CIF file result of SCXRD for the crystal structure at 300 K is shown in the Supporting Information. These results are consistent with those previously reported.[38] Figure 1 shows the crystal structure and thermal
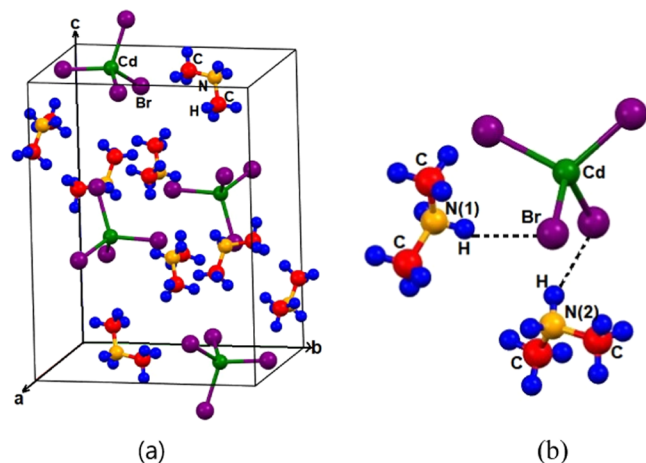

Figure 1. (a) Crystal structure and (b) thermal ellipsoids (50% probability) and numbering of the atoms for the structure of [NH$_2$(CH$_3$)$_2$]$_2$CdBr$_4$ at 300 K (CCDC number 2256555).

ellipsoids for each atom, and the XRD data for the [NH$_2$(CH$_3$)$_2$]$_2$CdBr$_4$ crystal are listed in Table 1. This compound is characterized by the N−H···Br hydrogen bonds connecting the two types of nonequivalent [NH$_2$(CH$_3$)$_2$](1) and [NH$_2$(CH$_3$)$_2$](2) cations to the [CdBr$_4$] anion. The average bond length for Cd−Br was 2.5815 Å, and those for nonequivalent N(1)−C and N(2)−C were 1.466 and 1.473 Å, respectively.

Table 1. Crystal Data and Structure Refinement for [NH$_2$(CH$_3$)$_2$]$_2$CdBr$_4$ at 300 K

chemical formula	C$_4$H$_{16}$N$_2$CdBr$_4$
weight	524.23
crystal system	monoclinic
space group	$P2_1/n$
T (K)	300
a (Å)	8.2528 (9)
b (Å)	11.7833 (14)
c (Å)	15.3589 (18)
β (°)	94.726 (4)
Z	4
V (Å^3)	1488.5
radiation type	Mo Kα
wavelength (Å)	0.71073
reflections collected	27,266
independent reflections	3667 (R_{int} = 0.0487)
goodness of fit on F^2	1.033
final R indices [$I \geq 2\sigma(I)$]	R_1 = 0.0313, wR_2 = 0.0593
R indices (all data)	R_1 = 0.0499, wR_2 = 0.0648

2.2. Phase Transition Temperatures. Figure 2 shows two strong endothermic peaks at 383 and 439 K with
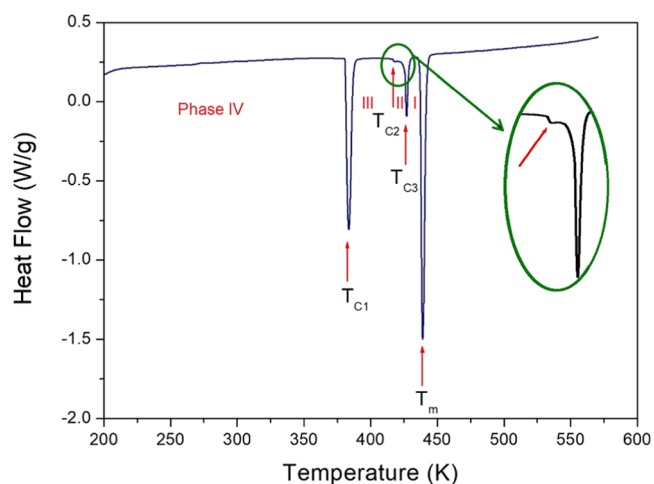

Figure 2. Differential scanning calorimetry curve of [NH$_2$(CH$_3$)$_2$]$_2$CdBr$_4$ measured at a heating rate of 10 °C/min. A small peak marked T_{C2} near T_{C3} is shown magnified in an elliptical shape.

enthalpies of 12.93 and 17.14 kJ/mol, respectively. A weak endothermic peak was observed at 427 K with an enthalpy of 3.21 kJ/mol. Additionally, a minor peak with an enthalpy of 79 J/mol was observed at 417 K near the 427 K peak, as shown in the magnified inset in Figure 2. Starting at 200 K, these four phases are denoted as phase IV (below 383 K), phase III (between 383 and 417 K), phase II (between 417 and 427 K), and phase I (above 427 K).

To determine whether these four endothermic peaks represent the phase transition or melting temperatures, the changes in the single crystal with increasing temperature were observed using an optical polarizing microscope. Up to 430 K, the single crystal remained almost unchanged, but the surface of the single crystal started to melt above 439 K.

Additionally, powder XRD experiments were performed with increasing temperature in the measurement range of 5−

65° (2θ), as shown in Figure 3. The XRD powder patterns recorded below 380 K (black) differed from those recorded
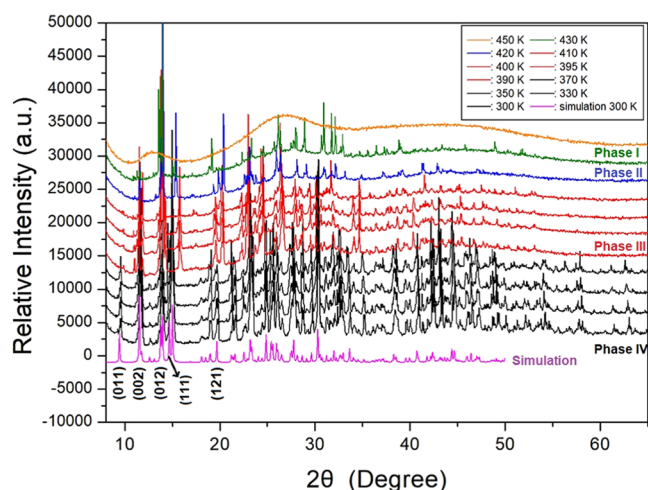

Figure 3. Powder X-ray diffraction patterns of $[NH_2(CH_3)_2]_2CdBr_4$ at phases IV (black), III (red), II (blue), and I (green). XRD pattern of 450 K (orange) is for the melting temperature. And, the simulation XRD pattern at 300 K is displayed in magenta color.

above 390 K (red). This difference is related to the structural phase transition at T_{C1} (383 K). Furthermore, the XRD patterns recorded above 390 K differed from those recorded at 420 K (blue). Moreover, the XRD pattern recorded at 420 K differed from that obtained at 430 K (olive), exhibiting a distinct change. Finally, the pattern at 450 K was completely different from those at temperatures below 450 K, and no crystallinity was observed, indicating that it is the melting point. Additionally, the simulated XRD pattern based on the CIF file at 300 K is shown in Figure 3, which agrees well with the experimental pattern. The peaks observed in this diffractogram are indexed with Mercury program.

The phase transition and melting temperatures determined by the powder XRD and optical polarizing microscope results are consistent with the endothermic peaks obtained from the DSC curves. Therefore, based on the DSC, XRD, and polarizing microscopy results, the phase transition temperatures are T_{C1} = 383 K, T_{C2} = 417 K, and T_{C3} = 427 K, and the melting temperature is T_m = 439 K.

2.3. Thermal Property. The TGA curve of the $[NH_2(CH_3)_2]_2CdBr_4$ crystal with increasing temperature is shown in Figure 4. The partial decomposition temperature was observed at 547 K, corresponding to a weight loss of 2%. Therefore, this material is thermally stable up to 547 K. The molecular weight of the $[NH_2(CH_3)_2]_2CdBr_4$ crystal decreased rapidly as the temperature increased owing to partial decomposition. From the total molecular weight of 524.23 mg, the amounts remaining after partial decomposition of HBr and 2HBr were obtained using the TGA data and the following chemical reactions:[45]
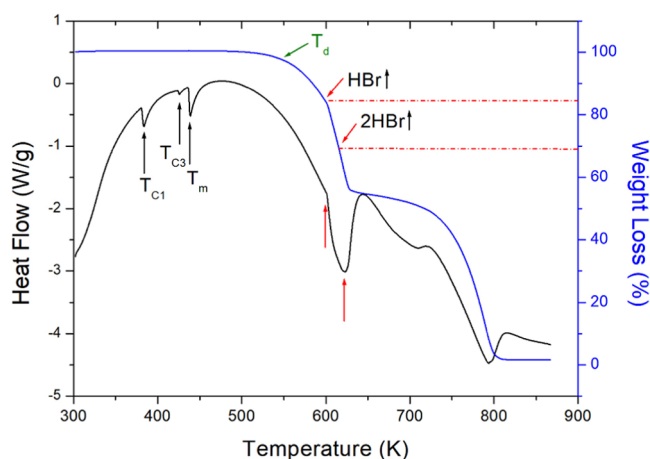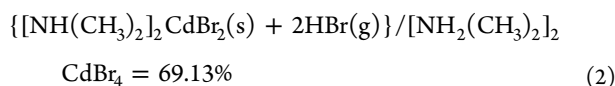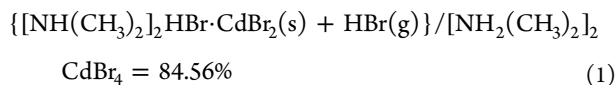
$$\{[NH(CH_3)_2]_2 HBr \cdot CdBr_2(s) + HBr(g)\}/[NH_2(CH_3)_2]_2$$
$$CdBr_4 = 84.56\% \qquad (1)$$

$$\{[NH(CH_3)_2]_2 CdBr_2(s) + 2HBr(g)\}/[NH_2(CH_3)_2]_2$$
$$CdBr_4 = 69.13\% \qquad (2)$$

Figure 4. Thermogravimetric analysis and differential thermal analysis curves of $[NH_2(CH_3)_2]_2CdBr_4$.

Molecular weight losses of 25 and 31% were observed after decomposition of HBr and 2HBr, respectively. The initial weight loss (25%) occurred in the temperature range of 550−600 K, and the second decomposition (31%) occurred in the temperature range of 623 K.

In contrast, three endothermic peaks were observed at 383, 425, and 438 K in the differential thermal analysis (DTA) curve, which is the differential form of the TGA curve, and are in good agreement with the phase transition and melting temperatures determined by DSC. The large endothermic peak observed near 623 K is in good agreement with the 2HBr decomposition temperature calculated from the total weight of the crystal. Moreover, total weight loss occurred at temperatures above 800 K.

2.4. ^{1}H and ^{13}C MAS NMR Chemical Shifts. The in situ NMR chemical shifts for ^{1}H in the $[NH_2(CH_3)_2]_2CdBr_4$ crystal were recorded for phases IV, III, and II, as shown in Figure 5. For phase IV, the ^{1}H NMR signals of NH$_2$ and CH$_3$

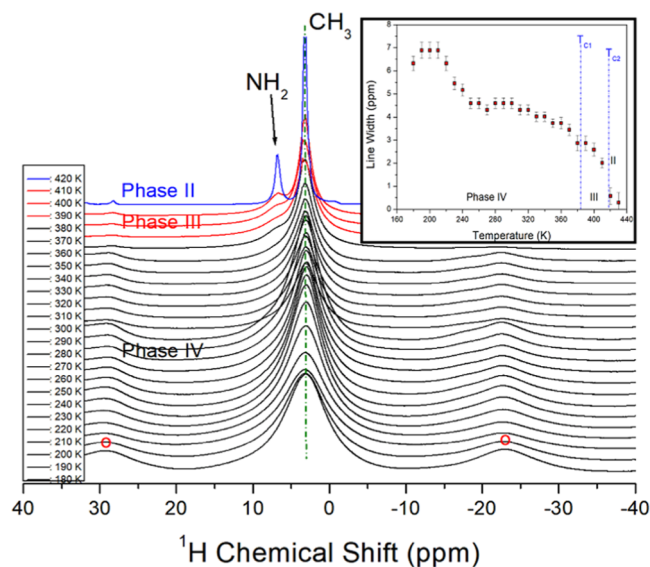**Figure 5.** In situ ^{1}H MAS NMR chemical shifts of NH$_2$ and CH$_3$ in $[NH_2(CH_3)_2]_2CdBr_4$ at phases IV, III, and II. And, the open circles are the sidebands for ^{1}H in CH$_3$ (inset: change of linewidth as a function of temperature).

completely overlapped, and only one signal was obtained. The sidebands in the ^{1}H spectrum for phase IV are represented by open circles. The ^{1}H chemical shifts barely changed as the temperature increased, whereas the ^{1}H signals of NH$_2$ and CH$_3$ for phase III began to separate. The ^{1}H coordination geometry for NH$_2$ changed near T_{C1}. These results indicate that the ^{1}H coordination geometry for CH$_3$ remains unchanged with increasing temperature, whereas that for NH$_2$ changes.

Conversely, the full width at half-maximum of the ^{1}H NMR signal decreased with increasing temperature, as shown in detail in Figure 5. The linewidth of the ^{1}H NMR signal decreased from approx. 7 to 1 ppm as the temperature increased and showed a distinct decrease at T_{C2}, similar to the change in ^{1}H chemical shifts. This trend indicates that the mobility of ^{1}H becomes very active at high temperatures.

Additionally, the in situ ^{13}C NMR chemical shifts in [NH$_2$(CH$_3$)$_2$]$_2$CdBr$_4$ were measured for phases IV, III, and

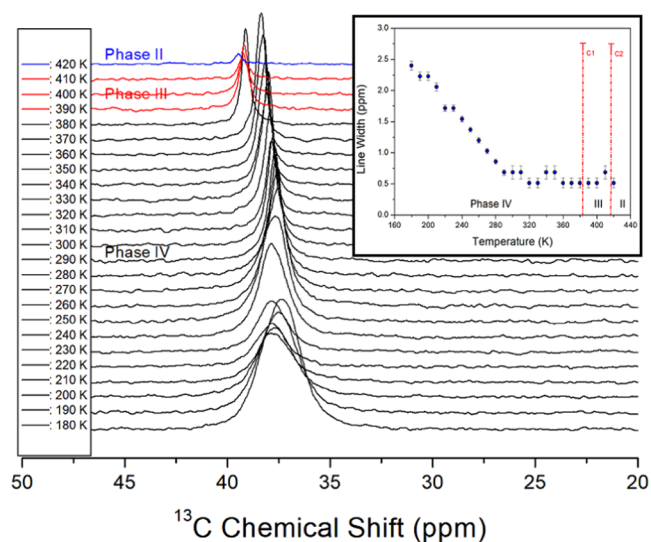**Figure 6.** In situ ^{13}C MAS NMR chemical shifts in [NH$_2$(CH$_3$)$_2$]$_2$CdBr$_4$ at phases IV, III, and II (inset: change of linewidth as a function of temperature).

II with increasing temperature, as shown in Figure 6. Only one ^{13}C signal was observed for the two CH$_3$ groups in the crystal structure; thus, the structural environments for these two CH$_3$ groups are identical. The ^{13}C NMR chemical shift obtained at 300 K was observed at 37.84 ppm. The chemical shifts for phases IV and III shifted in the positive direction, and the ^{13}C chemical shifts discontinuously changed near T_{C1}, similar to the ^{1}H NMR results. The linewidths shown in the inset in Figure 6 were very small compared to the ^{1}H linewidths, and the linewidths decreased with increasing temperature but remained almost constant at temperatures above 280 K.

2.5. Static ^{14}N and ^{113}Cd NMR Chemical Shifts. The static NMR spectrum for ^{14}N in NH$_2$ at the center of the cation in the [NH$_2$(CH$_3$)$_2$]$_2$CdBr$_4$ single crystal is shown in Figure 7. NMR spectra were obtained in the temperature range of 180–380 K, and the direction of the magnetic field and single crystal were measured in an arbitrary direction. The spin number of ^{14}N is $I = 1$, and therefore two resonance signals were expected owing to the quadrupole interaction.[46] Notably, it was very difficult to obtain ^{14}N NMR spectra owing to the
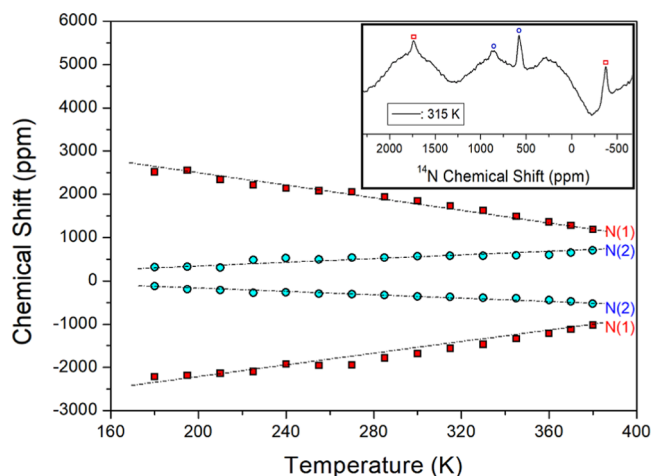
Figure 7. Static ^{14}N NMR chemical shifts in [NH$_2$(CH$_3$)$_2$]$_2$CdBr$_4$ as functions of temperature. The peaks indicated by the red squares are for N(1) site and the peaks indicated by the blue circles are for N(2) site (inset: ^{14}N NMR spectrum at 315 K).

low Larmor frequency. Because the intensity was very weak and the linewidth was broad, it was difficult to obtain the ^{14}N NMR signals, as shown in Figure 7. The [NH$_2$(CH$_3$)$_2$]$_2$CdBr$_4$ structure consists of complex [CdBr$_4$] anions, and [NH$_2$(CH$_3$)$_2$](1) and [NH$_2$(CH$_3$)$_2$](2) cations. The structural properties of N(1) and N(2) in the two [NH$_2$(CH$_3$)$_2$]$^+$ groups were determined based on the ^{14}N NMR chemical shifts. The chemical shifts of the ^{14}N NMR spectra obtained at several temperatures are shown in Figure 7. The N(1) chemical shifts represented by red squares decreased with increasing temperature, whereas the N(2) chemical shifts represented by blue circles slightly increased. The pairs for ^{14}N are indicated by the same symbols, and N(1) and N(2) were arbitrarily named. The linewidth at 300 K was very broad at approximately 80 ppm. However, ^{14}N signals were not easily detected at temperatures near T_{C1}. The two groups of ^{14}N signals demonstrate the presence of two nonequivalent N sites. Additionally, it was confirmed that there were different N(1) and N(2) sites, as shown in the single-crystal XRD results. The continuous change in the N(1) and N(2) chemical shifts with increasing temperature indicates a change in the coordination geometry of the local environment of N.

Based on the information obtained from ^{113}Cd chemical shifts, the changes in the structural environment around Cd in the anion CdBr$_4$ were evaluated. The spin number of ^{113}Cd is $I = 1/2$, and therefore only one resonance signal was expected.[46] The static ^{113}Cd NMR chemical shifts of the three phases are shown in Figure 8. The chemical shift of ^{113}Cd at 300 K was 386.93 ppm, and the linewidth was broad at approx. 30 ppm. ^{113}Cd NMR spectra measured at 180 and 420 K are shown in the inset in Figure 8. The linewidth at 180 K was much wider than that at 420 K, indicating that the mobility of Cd increases with increasing temperature. In contrast to the ^{1}H and ^{13}C chemical shifts, the ^{113}Cd chemical shifts continuously changed toward negative values, and the chemical shifts near T_{C1} showed discontinuous variation. Based on these results, it is proposed that the change in Br closest to Cd is large.

2.6. ^{1}H and ^{13}C NMR Spin–Lattice Relaxation Times. To obtain the spin–lattice relaxation time $T_{1\rho}$, the intensities of the NMR signals in the ^{1}H and ^{13}C NMR spectra were measured with increasing delay times. The decay curves of the
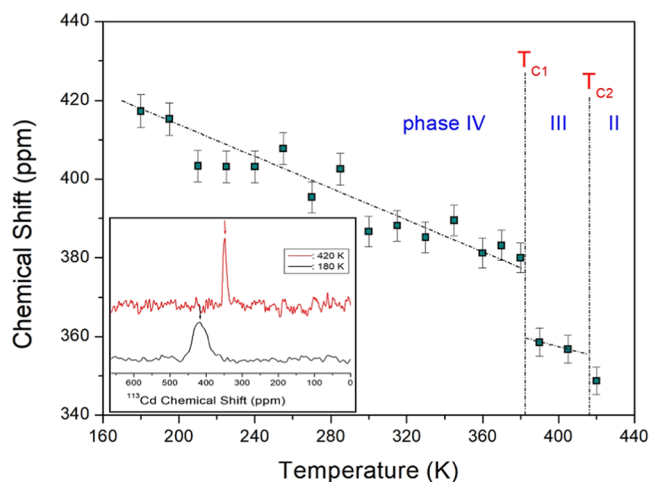
Figure 8. Static ^{113}Cd NMR chemical shifts in $[NH_2(CH_3)_2]_2CdBr_4$ at phases IV, III, and II (inset: ^{113}Cd NMR spectrum at 180 K and 420 K).

change in the signal intensities and delay times are expressed by the following equation[46−48]

$$I(t) = I(0)\exp(-t/T_{1\rho}) \tag{3}$$

where $I(t)$ is the intensity of the spectrum at time t and $I(0)$ is the intensity of the spectrum at time $t = 0$. The $T_{1\rho}$ values for ^{1}H and ^{13}C in $[NH_2(CH_3)_2]_2CdBr_4$ were obtained using eq 3, and the results are shown in Figures 9 and 10 as a function of
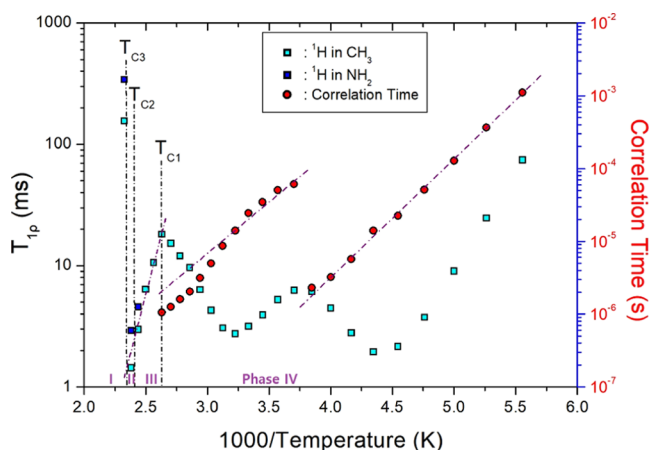

Figure 9. ^{1}H NMR spin-lattice relaxation times $T_{1\rho}$ in $[NH_2(CH_3)_2]_2CdBr_4$ at phases IV, III, II, and I (inset: the slopes of dotted lines are represented as the activation energies by the correlation times as a function of inverse temperature).

inverse temperature. The chemical shifts for ^{1}H in NH$_2$ and CH$_3$ were almost independent of temperature, but the $T_{1\rho}$ values were strongly dependent on temperature. As the temperature increased, $T_{1\rho}$ rapidly decreased, exhibiting a minimum value of 1.95 ms at 230 K and a second minimum value of 2.74 ms at 310 K. Additionally, $T_{1\rho}$ was rapidly decreased at temperatures above T_{C1} and then rapidly increased at temperatures above T_{C3}. The $T_{1\rho}$ values of ^{1}H have two minima at 230 and 310 K, indicating molecular motion according to the Bloembergen−Purcell−Pound (BPP) theory. These $T_{1\rho}$ minima are attributable to the reorientational motion of ^{1}H in NH$_2$ and CH$_3$. Therefore, the
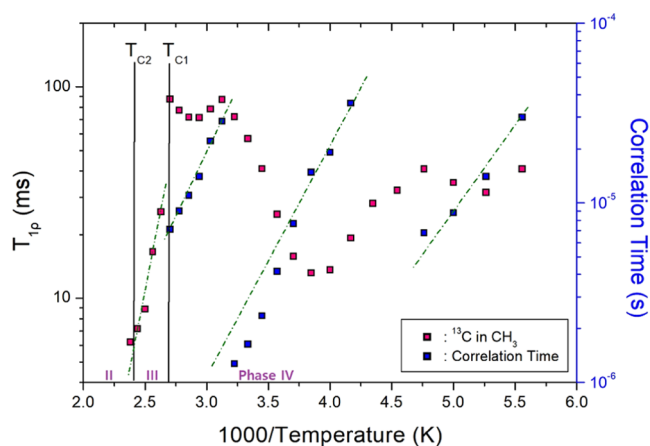
experimental value of $T_{1\rho}$ can be expressed by the correlation time τ_C for molecular motion, where the τ_C value is determined as follows:[44,46]

$$
\begin{aligned}
(1/T_{1\rho}) = R\{ & 4\tau_C/[1 + \omega_1^2\tau_C^2] + \tau_C \\
& /[1 + (\omega_C - \omega_H)^2\tau_C^2] + 3\tau_C/[1 + \omega_C^2\tau_C^2] \\
& + 6\tau_C/[1 + (\omega_C + \omega_H)^2\tau_C^2] \\
& + 6\tau_C/[1 + \omega_H^2\tau_C^2]\}
\end{aligned}
\tag{4}
$$

where R is a constant, ω_1 is the spin-lock field, and ω_C and ω_H are the Larmor frequencies for carbon and protons, respectively. The data were analyzed by assuming that $T_{1\rho}$ had the lowest value when $\omega_1\tau_C = 1$, and the relationship between $T_{1\rho}$ and the radio frequency power of the spin-lock pulse ω_1 was applicable. Because the $T_{1\rho}$ curves exhibited minima, the coefficient R in eq 4 can be obtained. Based on the obtained value for R, the τ_C values were calculated as a function of temperature. The local field fluctuation is owing to the thermal motion of protons and carbon atoms, which are activated by thermal energy. The τ_C of motion is generally assumed to have Arrhenius dependence on the activation energy for motion and temperature.[44,46]

$$\tau_C = \tau_C°\exp(-E_a/k_BT) \tag{5}$$

where E_a and k_B are the activation energy of motion and the Boltzmann constant, respectively. The magnitude of E_a depends on the molecular dynamics. To determine the molecular dynamics, the logarithmic scale of τ_C represented by red circles as a function of $1000/T$ is shown in Figure 9. Based on the slopes of the dotted lines at low and high temperatures for phase IV, E_a was found to be 31.78 ± 3.41 and 27.88 ± 2.45 kJ/mol, respectively. Additionally, the E_a value obtained from the slope of $T_{1\rho}$ as a function of inverse temperature for phase III was 72.12 ± 0.84 kJ/mol. Therefore, the difference in E_a between phases IV and III near T_{C1} was very large.

For ^{13}C, the $T_{1\rho}$ values shown in Figure 10 changed significantly at the phase transition temperature of T_{C1}. As the temperature increased, $T_{1\rho}$ exhibited a small minimum value of 18.22 ms at 190 K, a second minimum value of 13.18 ms at 260 K, and a third minimum value of 71.49 ms at 340 K.

Figure 10. ^{13}C NMR spin-lattice relaxation times $T_{1\rho}$ in $[NH_2(CH_3)_2]_2CdBr_4$ at phases IV, III, and II (inset: the slopes of dotted lines are represented as the activation energies by the correlation times as a function of inverse temperature).

Moreover, $T_{1\rho}$ was rapidly shortened at temperatures above T_{C1}. The $T_{1\rho}$ values of ^{13}C exhibited three minima at 190, 260, and 340 K, indicating that molecular motion occurs according to the BPP theory. These minimum values of $T_{1\rho}$ are clearly attributable to the reorientational motion of ^{13}C in CH_3. The experimental values of $T_{1\rho}$ were expressed in terms of the τ_C. The logarithmic scale of τ_C represented by blue squares as a function of $1000/T$ is shown in Figure 10. Based on the slopes of the dotted line at low and high temperatures for phase IV, E_a was found to be 18.22 ± 3.41, 21.07 ± 2.45, and 28.78 kJ/mol, respectively. Additionally, the E_a value obtained from the slope of $T_{1\rho}$ as a function of inverse temperature for phase III was 55.66 ± 0.84 kJ/mol. Therefore, the difference in E_a between phases IV and III near T_{C1} was very large, which is similar to the ^1H results.

3. CONCLUSIONS

The physicochemical properties of the organic−inorganic hybrid $[NH_2(CH_3)_2]_2CdBr_4$ crystal are discussed. First, the monoclinic structure of this crystal was confirmed by single-crystal XRD, and the three-phase transition temperatures of 383, 417, and 427 K were determined using DSC and powder XRD analyses. This crystal had a good thermal stability of approximately 547 K, and weight loss was observed with increasing temperature owing to thermal decomposition, which resulted in the loss of HBr and 2HBr moieties. Second, the chemical shifts were caused by the local field around the resonating nucleus. Moreover, the ^1H, ^{13}C, ^{14}N, and ^{113}Cd NMR chemical shifts changed continuously with temperature, especially at T_{C1}, suggesting that the local environment changed with temperature. Owing to the large change in ^{113}Cd chemical shifts, the coordination geometry of Br around Cd in $CdBr_4$ tetrahedra changes near T_{C1}. Therefore, it is known that Br plays an important role in the N−H···Br hydrogen bond.[49−52] Finally, ^1H $T_{1\rho}$ and ^{13}C $T_{1\rho}$ values, which represent the energy transfer around the ^1H and ^{13}C atoms of the cation, changed significantly with temperature, indicating that the $T_{1\rho}$ values for ^1H and ^{13}C are governed by tumbling motions. The activation energies derived from the results of the NMR $T_{1\rho}$ experiments for molecular motion were very high at high temperatures. Based on the basic mechanism obtained for the $[NH_2(CH_3)_2]_2CdBr_4$ crystal, it is expected that the application of this organic−inorganic material is possible.

4. EXPERIMENTAL SECTION

4.1. Crystal Growth. Single crystals of $[NH_2(CH_3)_2]_2CdBr_4$ were synthesized using dimethylammonium bromide (Aldrich, 98%) and $CdBr_2·4H_2O$ (Aldrich, 98%) in a ratio of 2:1. The mixture was stirred and heated to obtain a homogeneous solution. Subsequently, the mixture was filtered through a filter paper, and transparent colorless single crystals were grown by gradual evaporation for a few days in a temperature-controlled oven at 300 K.

4.2. Characterization. The structure and lattice parameters of the $[NH_2(CH_3)_2]_2CdBr_4$ crystal were determined at 300 K using a single-crystal XRD system at the Korea Basic Science Institute (KBSI) Western Seoul Center. Powder XRD patterns were measured at several temperatures at the same facility. The experimental conditions for the two XRD measurements are described in previously reported results.[45]

DSC measurements were performed on a DSC instrument (TA Instruments, DSC 25) in the temperature range of 200−573 K at a heating rate of 10 K/min under nitrogen gas flow. The amount of sample used in the DSC experiment was 6.3 mg.

Additionally, TGA was performed in the temperature range of 300−873 K at a heating rate of 10 K/min under nitrogen gas flow.

The MAS NMR chemical shifts and spin-lattice relaxation time $T_{1\rho}$ of the $[NH_2(CH_3)_2]_2CdBr_4$ crystals were measured using a solid-state NMR spectrometer (AVANCE III+, Bruker) at the KBSI Western Seoul Center. The Larmor frequency for the ^1H NMR experiment was 400.13 MHz, and that for the ^{13}C NMR experiment was 100.61 MHz. MAS NMR measurements of the samples in cylindrical zirconia rotors were performed at a spinning rate of 10 kHz to reduce the spinning sideband. Chemical shifts were referenced to standard materials adamantane and tetramethylsilane (TMS) for ^1H and ^{13}C, respectively, to accurately measure the chemical shifts of the samples. $T_{1\rho}$ values were measured using a $\pi/2 - \tau$ pulse with a spin-lock pulse of duration τ. Static ^{14}N NMR chemical shifts were recorded using the one-pulse method at a Larmor frequency of 28.90 MHz, and NH_4NO_3 was used as the standard sample. Furthermore, static ^{113}Cd NMR chemical shifts were measured at a Larmor frequency of 88.75 MHz, and the chemical shift of $CdCl_2O_8·6H_2O$ was used as the standard sample.

■ ASSOCIATED CONTENT

ⓈI Supporting Information

The Supporting Information is available free of charge at https://pubs.acs.org/doi/10.1021/acsomega.3c05963.

$[NH_2(CH_3)_2]_2CdBr_4$ 300 K (CIF)

Accession Codes

Datasets generated and/or analyzed during the current study are available in the CCDC 2256555.

■ AUTHOR INFORMATION

Corresponding Author

Ae Ran Lim − *Graduate School of Carbon Convergence Engineering, Jeonju University, Jeonju 55069, Korea; Department of Science Education, Jeonju University, Jeonju 55069, Korea;* ⓞ orcid.org/0000-0002-5242-9189; Phone: +82-(0)63-220-2514; Email: arlim@jj.ac.kr, aeranlim@hanmail.net

Authors

Sun Ha Kim − *Seoul Western Center, Korea Basic Science Institute, Seoul 03759, Korea; Department of Chemistry, Kyungpook National University, Daegu 41566, Korea*

Yong Lak Joo − *School of Chemical and Biomolecular Engineering, Cornell University, Ithaca, New York 14853, United States;* ⓞ orcid.org/0000-0002-4646-1625

Complete contact information is available at:
https://pubs.acs.org/10.1021/acsomega.3c05963

Notes

The authors declare no competing financial interest.

■ REFERENCES

(1) Mathlouthi, M.; Valkonen, A.; Rzaigui, M.; Smirani, W. Structural characterization, spectroscopic, thermal, AC conductivity and dielectric properties and antimicrobial studies of $(C_8H_{12}N)_2[SnCl_6]$. *Phase Transitions* **2017**, *90*, 399−414.

(2) Gao, Y.-F.; Zhang, T.; Zhang, W.-Y.; Ye, Q.; Fu, D.-W. Great advance in high T_c for hybrid photoelectric-switch bulk/film coupled with dielectric and blue-white light. *J. Mater. Chem. C* **2019**, *7*, 9840−9849.

(3) Nie, Y.; Zhang, Z.-X.; Shi, P.-P.; Zhang, W.-Y.; Q, Y.; Fu, D.-W. Felxible Thin Film and Bulk Switchable Relaxor Coexisting Most Optimal 473 nm Blue Light without Blue-Light Hazard/Visual Injury. *J. Phys. Chem. C* **2019**, *123*, 28385−28391.

(4) Hua, X.-N.; Gao, J.-X.; Zhang, T.; Chen, X.-G.; Sun, D.-S.; Zhang, Y.-Z.; Liao, W.-Q. Switchable Dielectric Phase Transition with Drastic Symmetry Breaking in an Sn(IV)-Based Perovskite-Type Halide Semiconductor. *J. Phys. Chem. C* **2019**, *123*, 21161−21166.

(5) Wang, Z.-X.; Zhang, H.; Wang, F.; Cheng, H.; He, W.-H.; Liu, Y.-H.; Huang, X.-Q.; Li, P.-F. Superior Transverse Piezoelectricity in a Halide Perovskite Molecular Ferroelectric Thin Film. *J. Am. Chem. Soc.* **2020**, *142*, 12857−12864.

(6) Chen, X.-G.; Song, X.-J.; Zhang, Z.-X.; Li, P.-F.; Ge, J.-Z.; Tang, Y.-Y.; Gao, J.-X.; Zhang, W.-Y.; Fu, D.-W.; You, Y.-M.; Xiong, R.-G. Two-Dimensional Layered Perovskite Ferroelectric with Giant Piezoelectric Voltage Coefficient. *J. Am. Chem. Soc.* **2020**, *142*, 1077−1082.

(7) Maczka, M.; Ptak, M.; Gagor, A.; Stefanska, D.; Zareba, J. K.; Sieradzki, A. Methylhydrazinium Lead Bromide: Noncentrosymmetric Three-Dimensional Perovskite with Exceptionally Large Framework Distortion and Green Photoluminescence. *Chem. Mater.* **2020**, *32*, 1667−1673.

(8) Zeng, Y.-L.; Huang, X.-Q.; Huang, C.-R.; Zhang, H.; Wang, F.; Wang, Z.-X. Unprecedented 2D Homochiral Hybrid Lead-Iodide Perovskite Thermochromic Ferroelectrics with Ferroelastic Switching. *Angew. Chem., Int. Ed.* **2021**, *60*, 10730−10735.

(9) Mączka, M.; Zareba, J. K.; Gagor, A.; Stefanska, D.; Ptak, M.; Roleder, K.; Kajewski, D.; Soszynski, A.; Fedoruk, K.; Sieradzki, A. [Methylhydrazinium]$_2$PbBr$_4$, a Ferroelectric Hybrid Organic-Inorganic Perovskite with Multiple Nonlinear Optical Outputs. *Chem. Mater.* **2021**, *33*, 2331−2342.

(10) Han, K.; Ye, X.; Li, B.; Wei, Z.; Wei, J.; Wang, P.; Cai, H. Organic-Inorganic Hybrid Compound [H$_2$-1,5-Diazabicyclo[3.3.0]-octane]ZnBr$_4$ with Reverse Symmetry Breaking Shows a Switchable Dielectric Anomaly and Robust Second Harmonic Generation Effect. *Inorg. Chem.* **2022**, *61*, 11859−11865.

(11) Zhang, H.; Tan, Y.-H.; Tang, Y.-Z.; Fan, X.-W.; Peng, X.-L.; Han, R.-R.; Li, Y.-K.; Wang, F.-X. Two Manganese(II)-Based Hybrid Multifunctional Phase Transition Materials with Strong Photoluminescence, High Quantum Yield, and Switchable Dielectric Properties: $(C_6NH_{16})_2MnBr_4$ and $(C_7H_{18})_2MnBr_4$. *Inorg. Chem.* **2022**, *61*, 10454−10460.

(12) Hermes, I. M.; Bretschneider, S. A.; Bergmann, V. W.; Li, D.; Klasen, A.; Mars, J.; Tremel, W.; Laquai, F.; Butt, H.-J.; Mezger, M.; Berger, R.; Rodriguez, B. J.; Weber, S. A. L. Ferroelastic Fingerprints in Methylammonium Lead Iodide Perovskite. *J. Phys. Chem. C* **2016**, *120*, 5724−5731.

(13) Abdel-Aal, S. K.; Abdel-Rahman, A. S.; Kocher-Oberlehner, G. G.; Ionov, A.; Mozhchil, R. Structure, optical studies of 2D hybrid perovskite for photovoltaic applications. *Acta Crystallogr., Sect. A: Found. Adv.* **2017**, *70*, No. C1116.

(14) Strelcov, E.; Dong, Q.; Li, T.; Chae, J.; Shao, Y.; Deng, Y.; Gruverman, A.; Huang, J.; Centrone, A. CH$_3$NH$_3$PbI$_3$ perovskites: Ferroelasticity revealed. *Sci. Adv.* **2017**, *3*, No. e1602165.

(15) Liu, Y.; Collins, L.; Proksch, R.; Kim, S.; Watson, B. R.; Doughty, B.; Calhoun, T. R.; Ahmadi, M.; Ievlev, A. V.; Jesse, S.; Retterer, S. T.; Belianinov, A.; Xiao, K.; Huang, J.; Sumpter, B. G.; Kalinin, S. V.; Hu, B.; Ovchinnikova, O. S. Chemical nature of ferroelastic twin domains in CH$_3$NH$_3$PbI$_3$ perovskite. *Nat. Mater.* **2018**, *17*, 1013−1019.

(16) Lee, J.; Lee, W.; Kang, K.; Lee, T.; Lee, S. K. Layer-by-Layer Structural Identification of 2D Ruddlesden-Popper Hybrid Lead Iodide Perovskites by Solid-State NMR Spectroscopy. *Chem. Mater.* **2021**, *33*, 370−377.

(17) Negrier, P.; Couzi, M.; Chanh, N. B.; Hauw, C.; Meresse, A. Structural phase transitions in the perovskite-type layer compound NH$_3$(CH$_2$)$_5$NH$_3$CdCl$_4$. *J. Phys.* **1989**, *50*, 405−430.

(18) Mostafa, M. F.; El-Hakim, S. A. Structural Phase Transition and the Dielectric Permittivity of the Model Lipid Bilayer [(CH$_2$)$_{12}$(NH$_3$)$_2$]CuCl$_4$. *Phase Transitions* **2003**, *76*, 587−599.

(19) Mostafa, M. F.; Youssef, A. A. A. Magnetic and Electric Studies of a New Cu(II) Perovskite-like Material. *Z. Naturforsch. A* **2004**, *59*, 35−46.

(20) Rao, C. N. R.; Cheetham, A. K.; Thirumurugan, A. Hybrid inorganic−organic materials: a new family in condensed matter physics. *J. Phys.: Condens. Matter* **2008**, *20*, No. 83202.

(21) Arkenbout, A. H.; Uemura, T.; Takeya, J.; Palstra, T. T. M. Charge-transfer induced surface conductivity for a copper based inorganic-organic hybrid. *Appl. Phys. Lett.* **2009**, *95*, No. 173104.

(22) Pradeesh, K.; Yadav, G. S.; Singh, M.; Prakash, G. V. Synthesis, structure and optical studies of inorganic−organic hybrid semiconductor, NH$_3$(CH$_2$)$_{12}$NH$_3$PbI$_4$. *Mater. Chem. Phys.* **2010**, *124*, 44−47.

(23) Saikumar, I.; Ahmad, S.; Baumberg, J. J.; Prakash, G. V. Fabrication of excitonic luminescent inorganic−organic hybrid nano- and microcrystals. *Scr. Mater.* **2012**, *67*, 834−837.

(24) Staśkiewicz, B.; Czupinski, O.; Czapla, Z. On some spectroscopic properties of a layered 1,3-diammoniumpropylene tetrabromocadmate hybrid crystal. *J. Mol. Struct.* **2014**, *1074*, 723−731.

(25) Staśkiewicz, B.; Turowska-Tyrk, I.; Baran, J.; Gorecki, C.; Czapla, Z. Structural characterization, thermal, vibrational properties and molecular motions in perovskite-type diaminopropanetetrachlorocadmate NH$_3$(CH$_2$)$_3$NH$_3$CdCl$_4$ crystal. *J. Phys. Chem. Solids* **2014**, *75*, 1305−1317.

(26) Mostafa, M. F.; El-khiyami, S. S. Crystal structure and electric properties of the organic−inorganic hybrid: [(CH$_2$)$_6$(NH$_3$)$_2$]ZnCl$_4$. *J. Solid State Chem.* **2014**, *209*, 82−88.

(27) Lv, X.-H.; Liao, W.-Q.; Li, P.-F.; Wang, Z.-X.; Mao, C.-Y.; Zhang, Y. Dielectric and photoluminescence properties of a layered perovskite-type organic−inorganic hybrid phase transition compound: NH$_3$(CH$_2$)$_5$NH$_3$MnCl$_4$. *J. Mater. Chem. C* **2016**, *4*, 1881−1885.

(28) Przeslawski, J.; Czapla, Z.; Crofton, M.; Dacko, S. On the "inverted" phase transitions in ferroic crystals containing propylenediammonium cations. *Ferroelectrics* **2018**, *534*, 220−227.

(29) Narita, N.; Yamada, I. Nonlinear Magnetic-Susceptibility of Two-Dimensional Magnets $(C_nH_{2n+1}$ NH$_3$)$_2$CuCl$_4$ with n=1, 2 and 3. *J. Phys. Soc. Jpn.* **1996**, *65*, 4054−4061.

(30) Mitzi, D. B. Templating and structural engineering in organic−inorganic perovskites. *J. Chem. Soc., Dalton Trans.* **2001**, 1−12.

(31) Pradeesh, K.; Baumberg, J. J.; Prakash, G. V. Exciton switching and Peierls transitions in hybrid inorganic-organic self-assembled quantum wells. *Appl. Phys. Lett.* **2009**, *95*, No. 173305.

(32) Cheng, Z.; Lin, J. Layered organic−inorganic hybrid perovskites: structure, optical properties, film preparation, patterning and templating engineering. *CrystEngComm* **2010**, *12*, 2646−2662.

(33) Ahmad, S.; Hanmandlu, C.; Kanaujia, P. K.; Prakash, G. V. Direct deposition strategy for highly ordered inorganic organic perovskite thin films and their optoelectronic applications. *Opt. Mater. Express* **2014**, *4*, 1313−1323.

(34) González-Carrero, S.; Galian, R. E.; Perez-Prieto, J. Organometal Halide Perovskites: Bulk Low-Dimension Materials and Nanoparticles. *Part. Part. Syst. Charact.* **2015**, *32*, 709−720.

(35) Czapla, Z.; Przeslawski, J.; Crofton, M.; Janczak, J.; Czupinski, O.; Ingram, A.; Kostrzewa, M. Structural phase transition in a perovskite-type $NH_3(CH_2)_3NH_3CuCl_4$ crystal − X-ray and optical studies. *Phase Transitions* **2017**, *90*, 637−643.

(36) Abdel-Adal, S. K.; Kocher-Oberlehner, G.; Ionov, A.; Mozhchil, R. N. Effect of organic chain length on structure, electronic composition, lattice potential energy, and optical properties of 2D hybrid perovskites $[(NH_3)(CH_2)_n(NH_3)]CuCl_4$, $n = 2−9$. *Appl. Phys. A* **2017**, *123*, No. 531.

(37) Lim, A. R. Physicochemical properties of the cation in organic−inorganic perovskite $[NH_3(CH_2)_4(NH_3)]ZnBr_4$ crystals investigated using ^1H and ^{13}C nuclear magnetic resonance relaxation. *J. Solid State Chem.* **2021**, *302*, No. 122438.

(38) Waskowska, A. Crystal structure of dimethylammonium tetrabromocadmate (II). *Z. Kristallogr. - Cryst. Mater.* **1994**, *209*, 752−754.

(39) Horiuchi, K.; Ishihara, H.; Terao, H. Differential scanning calorimetry studies on structural phase transitions and molecular motions in $(CH_3NH_3)_2MBr_4$ and $[(CH_3)_2NH_2]_2MBr_4$ (M = Zn, Cd, and Hg). *J. Phys.: Condens. Matter* **2000**, *12*, No. 4799.

(40) Kim, N. H.; Choi, J. H.; Lim, A. R. Tumbling motions of $NH_2(CH_3)_2$ ions in $[NH_2(CH_3)_2]_2ZnCl_4$ studied using ^1H MAS NMR and ^{13}C CP/MAS NMR. *Solid State Sci.* **2014**, *38*, 103−107.

(41) Lim, A. R.; Paik, Y. Investigating the two inequivalent $NH_2(CH_3)_2$ ions in $[NH_2(CH_3)_2]_2CuCl_4$ using magic angle spinning nuclear magnetic resonance. *Solid State Sci.* **2017**, *65*, 61−67.

(42) Mahfoudh, N.; Karoui, K.; Gargouri, M.; BenRhaiem, A. Optical and electrical properties and conduction mechanism of $[(CH_3)_2NH_2]_2CoCl_4$. *Appl. Organomet. Chem.* **2020**, *34*, No. e5404.

(43) Mahfoudh, N.; Karoui, K.; Jomni, F.; BenRhaiem, A. Structural phase transition, thermal analysis, and spectroscopic studies in an organic−inorganic hybrid crystal: $[(CH_3)_2NH_2]_2ZnBr_4$. *Appl. Organomet. Chem.* **2020**, *34*, No. e5656.

(44) Mahfoudh, N.; Karoui, K.; BenRhaiem, A. Optical studies and dielectric response of $[DMA]_2MCl_4$ (M = Zn and Co) and $[DMA]_2ZnBr_4$. *RSC Adv.* **2021**, *11*, 24526−24535.

(45) Lim, A. R.; Kim, S. H.; Joo, Y. L. Physicochemical properties and structural dynamics of organic−inorganic hybrid $[NH_3(CH_2)_3NH_3]ZnX_4$ (X = Cl and Br) crystals. *Sci. Rep.* **2021**, *11*, No. 8408.

(46) Abragam, A. *Te Principles of Nuclear Magnetism*; Oxford University Press, 1961.

(47) Harris, R. K. *Nuclear Magnetic Resonance Spectroscopy*; Pitman Pub, 1983.

(48) Lim, A. R.; Cho, J. Growth, structure, phase transition, thermal properties, and structural dynamics of organic-inorganic hybrid $[NH_3(CH_2)_5NH_3]ZnCl_4$ crystal. *Sci. Rep.* **2022**, *12*, No. 16901.

(49) Ishihara, H.; Dou, S.-q.; Horiuchi, K.; Krishnan, V. G.; Paulus, H.; Fuess, H.; Weiss, A. Isolated versus condensed anion structure II; the influence of the cations (1,3-propanediammonium, 1,4-phenylendiammonium, and *n*-propylammonium) on structures and phase transitions of $CdBr_4^{2−}$ salts. A $^{79,81}Br$ NQR and X-ray structure analysis. *Z. Naturforsch.* **1996**, *51*, 1216−1228.

(50) Ishihara, H.; Dou, S.-q.; Horiuchi, K.; Paulus, H.; Fuess, H.; Weiss, A. Isolated versus condensed anion structure III; the influence of the cations 1,3-propanediammonium, 1,4-butanediammonium, and *n*-propylammonium, *n*-butylammonium and *n*-pentylammonium on structures and phase transitions of $ZnBr_4^{2−}$ salts. A ^{81}Br NQR and X-ray structure analysis. *Z. Naturforsch.* **1997**, *52*, 550−560.

(51) Mostafa, M. F.; Elkhiyami, S. S.; Alal, S. A. Discontinuous transition from insulator to semiconductor induced by phase change of the new organic-inorganic hybrid $[(CH_2)_7(NH_3)_2]CoBr_4$. *Mater. Chem. Phys.* **2017**, *199*, 454−463.

(52) Lim, A. R. Crystal structures, phase transitions, and nuclear magnetic resonance of organic-inorganic hybrid $[NH_2(CH_3)_2]_2ZnBr_4$ crystals. *RSC Adv.* **2023**, *13*, 1078−1084.